PHYSICAL REVIEW E **81**, 061601 (2010)

Phase-field-crystal model for fcc ordering

Kuo-An Wu,[*] Ari Adland, and Alain Karma
Department of Physics and Center for Interdisciplinary Research on Complex Systems, Northeastern University,
Boston, Massachusetts 02115, USA

(Received 8 January 2010; revised manuscript received 30 April 2010; published 23 June 2010)

We develop and analyze a two-mode phase-field-crystal model to describe fcc ordering. The model is formulated by coupling two different sets of crystal density waves corresponding to ⟨111⟩ and ⟨200⟩ reciprocal lattice vectors, which are chosen to form triads so as to produce a simple free-energy landscape with coexistence of crystal and liquid phases. The feasibility of the approach is demonstrated with numerical examples of polycrystalline and (111) twin growth. We use a two-mode amplitude expansion to characterize analytically the free-energy landscape of the model, identifying parameter ranges where fcc is stable or metastable with respect to bcc. In addition, we derive analytical expressions for the elastic constants for both fcc and bcc. Those expressions show that a nonvanishing amplitude of [200] density waves is essential to obtain mechanically stable fcc crystals with a nonvanishing tetragonal shear modulus $(C_{11}-C_{12})/2$. We determine the model parameters for specific materials by fitting the peak liquid structure factor properties and solid-density wave amplitudes following the approach developed for bcc [K.-A. Wu and A. Karma, Phys. Rev. B **76**, 184107 (2007)]. This procedure yields reasonable predictions of elastic constants for both bcc Fe and fcc Ni using input parameters from molecular dynamics simulations. The application of the model to two-dimensional square lattices is also briefly examined.

DOI: 10.1103/PhysRevE.81.061601 PACS number(s): 68.08.De, 61.72.Mm, 81.16.Rf

I. INTRODUCTION AND SUMMARY

The phase-field-crystal (PFC) method has emerged as an attractive computational approach to simulate the evolution of crystalline patterns [1–6]. By resolving the crystal density field, it naturally incorporates defects and elastic interactions arising from localized and large scale distortions of this field, respectively. Moreover, this method can in principle be used to simulate microstructural evolution on diffusive time scales that are much longer than typical time scales accessible by molecular dynamics (MD) simulations.

Like classical density-function theory (DFT), the PFC method is based on representing the free energy of a material by a functional of its density [7–14]. However, classical DFT and the PFC method use different functionals to achieve different goals. Classical DFT seeks a physically realistic mean-field description of the crystal density field $n(\vec{r})$ to reproduce quantitatively as accurately as possible the properties of a material. Since $n(\vec{r})$ is sharply peaked around mean atomic positions, this generally requires a very large number of terms in the traditional expansion of the number density as a sum of density waves

$$n(\vec{r}) = n_0\left(1 + \sum_i u_i e^{i\vec{K}_i\cdot\vec{r}}\right), \tag{1}$$

where each $\vec{K}_i$ represents a different reciprocal lattice vector (RLV) in this unrestricted sum. In contrast, by using a considerably simplified density functional, the PFC method essentially restricts this sum to a much smaller set of reciprocal lattice vectors in order to simulate efficiently the evolution of the crystal field on length and time scales as large as possible. Recent studies have shown that, despite this loss of realism, PFC models are able to reproduce quantitatively certain key properties that influence microstructural evolution such as the crystal-melt interfacial free-energy [15,16], the bulk modulus [16], and grain-boundary energies [16], which have been computed for the test case of pure Fe.

Despite this progress, the PFC method has only been developed for a small set of crystal structures. The original formulation of Elder *et al.* [1,2] uses the same free-energy functional as the Swift-Hohenberg model of pattern formation [17,18] of the form

$$\mathcal{F} = \int d\vec{r} f, \tag{2}$$

with the free-energy density

$$f = \frac{\phi}{2}[a + \lambda(q_0^2 + \nabla^2)^2]\phi + g\frac{\phi^4}{4}, \tag{3}$$

where ϕ represents the crystal density field. This one-mode model essentially truncates the sum Eq. (1) to one set of RLVs with equal magnitude $|\vec{K}_i| = q_0$ since higher K modes have much smaller amplitude. As a result, it favors crystal structures for which the principal RLVs can form "triads" (i.e., closed triangles), which include hexagonal and body-centered-cubic (bcc) ordering in two and three dimensions, respectively. Aside from favoring those structures, triad interactions are essential for solid-liquid coexistence. This is because in a weakly nonlinear expansion of the bulk free-energy density of the form, $f = c_2u^2 + c_3u^3 + c_4u^4 + \cdots$ (with $u_i = u$ for all principal RLVs), triads contribute a cubic term with a negative coefficient $c_3 < 0$. Since c_2 and c_4 are both positive, this cubic term is responsible for the existence of a free-energy barrier between the two minima of f corresponding to liquid $(u=0)$ and solid $(u_s > 0)$.

---

[*] Present address: Department of Materials Science and Engineering, Northwestern University, Evanston, IL 60208, USA.

In this paper, we use a "two-mode" phase-field-crystal model to model face-centered-cubic (fcc) structures, which has the free-energy density

$$f = \frac{\phi}{2}\{a + \lambda(\nabla^2 + q_0^2)^2[(\nabla^2 + q_1^2)^2 + r_1]\}\phi + g\frac{\phi^4}{4}. \qquad (4)$$

This model has the key property that it favors lattice structures composed of two sets of density waves with wave vector magnitudes equal to q_0 and q_1, respectively. In addition, the relative amplitudes of those density waves can be varied by varying r_1. A desired lattice structure is obtained by choosing $q_0 = |\vec{K}_i|$ and $q_1 = |\vec{K}_i'|$, respectively, where the first set corresponds in general to the principal RLVs of this lattice, and the second to some other set of RLVs with larger wave vector magnitude; all other RLVs have much smaller amplitude, thereby essentially truncating the sum Eq. (1) to two sets of RLVs. This construct provides more flexibility to form triad interactions by combining RLVs from those two sets, and hence to describe other crystal structures than bcc. We demonstrate this here for fcc ordering, which is obtained by choosing the sets $\{\vec{K}_i\}$ and $\{\vec{K}_i'\}$ to correspond to $\langle 111\rangle$ (principal set) and $\langle 200\rangle$ RLVs, respectively, with $q_1/q_0 = \sqrt{4/3}$. While there is in principle freedom in the choice of the second set $\{\vec{K}_i'\}$ for a given structure, we have chosen this set such that $q_1 > q_0$ is as small as possible, as desired for computational efficiency.

The form Eq. (4) reduces in the limit $r_1 = 0$ to the free-energy density introduced by Lifshitz and Petrich [19] as a generalization of the Swift-Hohenberg model to describe two-dimensional quasiperiodic patterns observed in Faraday wave experiments, which result from the superposition of two frequencies. Although formulated primarily to describe those patterns, this model was also shown to describe other patterns, including regular square crystal lattices in two dimensions with the choice $q_1/q_0 = \sqrt{2}$, which couples $\langle 10\rangle$ and $\langle 11\rangle$ RLVs.

The present introduction of the parameter r_1 in the form Eq. (4) provides the additional flexibility to change the relative stability of different crystal structures. This is because in the limit $r_1 \gg q_0^4$, this form reduces formally to the original Swift-Hohenberg form Eq. (3) after a simple rescaling of the parameters. Hence, as r_1 is increased the contribution of the second q_1-mode becomes less significant in comparison to the first q_0-mode. Consequently, as r_1 is increased from zero, the crystal structure favored by the two-mode interaction becomes metastable with respect to the one-mode structure. This added capability to model the coexistence of two different crystal structures, in addition to the coexistence of each structure with a liquid, should prove useful to model a wide range of phase transformations with a PFC approach. Fcc and bcc crystal structures have also been studied previously in the more quantitative framework of classical DFT with much larger sets of density waves [20–23].

In the next section, we scale the parameters of the model to write the free-energy functional in a dimensionless form with only three parameters: ϵ, which is the standard PFC model parameter analogous to temperature that controls the size of the solid-liquid coexistence regions as a function of density, $Q_1 \equiv q_1/q_0$, whose value is generally determined by the choice of crystal structure, and $R_1 \equiv r_1/q_0^4$ controls the relative stability of the two-mode and one-mode structures (fcc and bcc, respectively). In this section, we also use a standard common tangent construction to compute the phase diagram in the plane of density and ϵ for an illustrative choice of $R_1 = 0.05$. The phase diagram exhibits regions of bcc-liquid and fcc-liquid coexistence for small and large epsilon, respectively. The size of the fcc-liquid coexistence region depends generally on R_1. For $r_1 = 0$ where Eq. (4) reduces to the free-energy density of Lifshitz and Petrich [19], the analog phase diagram only exhibits fcc-liquid coexistence, so that a finite r_1 is necessary for the phase diagram to exhibit both bcc-liquid and fcc-liquid coexistence. We demonstrate the feasibility of the approach with some simulations of polycrystalline growth and (111) twin growth. A numerical computation of the (111) twin boundary energy for parameters of Ni is given in an Appendix. The ability to model twin growth is important for solidification modeling since twins can dramatically alter both eutectic [24,25] and dendritic [26] microstructures.

In Sec. III, we carry out an amplitude expansion of the bulk free-energy density in the small ϵ limit. This expansion exploits the property that, with the scaling $R_1 = \epsilon R$, the amplitudes of the $\langle 111\rangle$ and $\langle 200\rangle$ density waves scale as, $A_s \sim A\epsilon^{1/2}$ and $B_s \sim B\epsilon^{1/2}$, respectively, while the density difference between solid and liquid scales $\sim \epsilon^{3/2}$. Therefore, this density difference can be neglected in the small ϵ limit and the bulk free-energy density can be expressed solely in terms of those amplitudes. As required for solid-liquid coexistence, the free-energy density has minima in the (A,B) plane corresponding to liquid $(A = B = 0)$ and fcc solid (finite A and B values that depend on R). By comparing this form to the free-energy density for a single amplitude of bcc density waves (corresponding to $\langle 110\rangle$ RLVs), we identify different regions of relative fcc and bcc stability, which explains the phase diagram computed in Sec. II.

In Sec. IV, we discuss how to determine the two-mode PFC model parameters to relate them quantitatively to different materials. We follow essentially the same approach developed by two of the authors for the standard PFC one-mode model for bcc ordering [15]. For bcc, the parameters were completely determined by fitting three parameters: (i) the peak value of the liquid structure factor, $S(q_0)$, where $q_0 = |\vec{K}_{110}|$, (ii) the second derivative of the Fourier transform of the direct correlation function at this peak, $C''(q_0)$, and (iii) the solid-density wave amplitude u_{110}. For fcc, all the parameters except R_1 are determined by the same fit, where $q_0 = |\vec{K}_{111}|$. (The shape of the structure factor at $q_1 = |\vec{K}_{200}|$ is not realistically modeled given the limited number of model parameters.) R_1 then determines the ratio u_{200}/u_{111} of the $\langle 111\rangle$ and $\langle 200\rangle$ solid amplitudes, which can be varied to alter the relative stability of fcc and bcc.

In Sec. V, we derive analytical expressions for the three independent elastic constants of a cubic material, C_{11}, C_{12}, and C_{44}, for both the standard one-mode PFC model Eq. (3) and the present two-mode model Eq. (4). We use a brute force approach that consists of calculating to quadratic order the change of solid free-energy density, modeled by a one- or two-mode approximation for bcc and fcc, respectively, due to small dilation or shear transformations of the unit cell. We have checked that we obtain identical expressions to those derived recently by Spatschek and Karma for general lattices using an amplitude equation framework [27], which provides a nontrivial self-consistent test of our calculations. For the one-mode bcc model Eq. (3), the elastic constants are

$$\frac{C_{11}}{2} = C_{12} = C_{44} = -\frac{n_0 k_B T}{2} C''(q_0) q_0^2 u_{110}^2, \tag{5}$$

where $q_0 = |\vec{K}_{110}|$. For the two-mode fcc model (4),

$$C_{11} = -\frac{4 n_0 k_B T}{9} C''(q_0) q_0^2 (u_{111}^2 + 4 u_{200}^2), \tag{6}$$

and

$$C_{12} = C_{44} = -\frac{4 n_0 k_B T}{9} C''(q_0) u_{111}^2, \tag{7}$$

where $q_0 = |\vec{K}_{111}|$ and $R_1 = 0$ for simplicity.

Using values of $C''(q_0)$ and density wave amplitudes from molecular dynamics simulations for parameters of bcc Fe and fcc Ni, we find that the above expressions give reasonable estimates of elastic constants (e.g., $C_{11} \approx 90$ GPa for one-mode bcc PFC model compared to $C_{11} \approx 128$ GPa in MD Fe and $C_{11} \approx 113$ GPa for the two-mode fcc PFC model compared to $C_{11} \approx 155$ GPa in MD Ni). The predicted values generally tend to be lower than the constants computed from MD simulations, but such discrepancies are to be expected given the PFC models are based on one or two modes. The analytical predictions for the elastic constants allow us to draw two important general conclusions pertaining to the development of PFC models for different crystal structures and to the method used to determine the parameters of those models.

The first conclusion, which follows directly from Eqs. (6) and (7), is that the presence of the second mode, which corresponds to [200] density waves, is essential to obtain a physically meaningful set of elastic constants for fcc. Without this second mode ($u_{200} = 0$), Eqs. (6) and (7), predict that $C_{11} = C_{12} = C_{44}$. This implies that the tetragonal shear modulus $C' = (C_{11} - C_{12})/2$ vanishes, and that the system is mechanically marginally stable. Of course, these analytical expressions for the elastic constants neglects the contributions of higher modes that are present in a full solution of the PFC equations. However, those higher modes are generally small for the small values of ϵ corresponding to Fe and Ni parameters. Therefore, the contributions of those modes will generally be small and will not change qualitatively this picture.

Square lattices have also been studied in the context of both pattern formation and phase transitions using models with the same spatial gradient terms as in the standard PFC model and additional nonlinear terms such as $|\nabla\phi|^4$ and $\phi^2|\nabla\phi|^2$ [28–31]. However, those models do not yield physically realistic elastic properties in the small ϵ limit where the density wave structure is dominated by a single mode. As discussed in Sec. VI, simple cubic lattices and two-dimensional square lattices with realistic elastic properties can be obtained in this limit by coupling $\langle 10 \rangle$ and $\langle 11 \rangle$ density waves.

The second conclusion, which is general, is that the elastic constants are uniquely determined once the phase-field model parameters have been fitted to the peak liquid structure properties, which fixes $C''(q_0)$, and the solid-density wave amplitudes, as in the approach of Wu and Karma [15] summarized above. This also fixes the value of the elastic bulk modulus

$$K = \frac{C_{11} + 2C_{12}}{3}. \tag{8}$$

In general, the bulk modulus can also be defined from the thermodynamic relation

$$K = V\frac{\partial^2 F}{\partial V^2} = n^2 \frac{\partial^2 (F/V)}{\partial n^2}, \tag{9}$$

where F is the total free energy, V is the volume, and $n = N/V$ is the number density. The second equality in the last equation can in principle be used to compute the bulk modulus directly from the PFC solid free-energy curve (F/V versus n), without computing the elastic constants. For a perfect crystal without vacancy, Eqs. (8) and (9) should in principle predict the same bulk modulus. However, the two definitions can give different predictions for the PFC model because the number of atoms per peak of the crystal density field is not constrained to unity. While the average number of atoms per peak will also differ from unity in a real crystal with vacancies, thereby altering the open-system elastic constants [32], the vacancy concentration is generally very small even at melting. How to meaningfully relate the predictions of Eqs. (8) and (9) for the bulk modulus is unclear in the PFC approach that, by construct, does not use a realistic description of the crystal density field, and also does not model vacancy formation explicitly.

Despite these limitations of the PFC approach, Jaatinen *et al.* [16] have recently proposed a modified one-mode PFC model to remedy the fact that, for the standard one-mode PFC model with the free-energy density Eq. (3), the bulk modulus predicted by Eq. (9) is several times smaller than the experimental value for parameters of bcc Fe. Their model yields a value of the bulk modulus computed through Eq. (9) that is in better agreement with experiment and also gives an improved prediction of the density difference between solid and liquid. It gives similar predictions of crystal-melt interfacial free energies for bcc Fe as obtained previously by Wu and Karma using the standard one-mode model [15].

In the light of Eq. (5), it is apparent that any one-mode model that fits the correct peak structure factor properties and solid-density wave amplitudes should predict the same elastic constants. This is consistent with the fact that Eq. (5) predicts a shear modulus $C_{44} \approx 45$ GPa for the standard one-mode model of bcc Fe, which is reasonably close to the value $C_{44} \approx 53$ GPa estimated by Jaatinen *et al.* [16] from numerical shearing experiments in their model for similar input parameters.

Since elastic constants are a major determinant of grain-boundary energies and long-range interactions between crystal defects, reproducing those constants, and hence, the bulk modulus predicted by Eq. (8), appears essential for modeling microstructural evolution. Also requiring that Eq. (9) predicts the correct bulk modulus using the solid free-energy curve may appear desirable. However, the motivation for doing so in the context of simple PFC models is somewhat less clear given the lack of realism of the crystal density field and the fact that Eqs. (5)–(7) predict reasonable values of the elastic constants. In fact, any one- or two-mode model with the same peak liquid structure factor properties and density wave amplitudes will predict essentially the same elastic constants associated with the free-energy cost of lattice distortions, and also the same interfacial energies as can be inferred from amplitude equations [15]. Since those elastic constants and interfacial energies determine predominantly thermodynamic driving forces for microstructural evolution in a PFC context, we have not found it necessary to formulate the two-mode PFC model in such a way that the bulk modulus is also correctly predicted from the solid free-energy curve using Eq. (9). Accordingly, we follow essentially the same approach outlined in Ref. [15] for determining the PFC model parameters. Finally, we only model quantitatively equilibrium properties in the present paper and time evolutions of polycrystalline microstructures are mainly shown for illustrative purposes.

II. PHASE-FIELD-CRYSTAL MODEL

A. Basic equations and scalings

The PFC equations have the standard form for conserved dynamics

$$\frac{\partial \phi}{\partial \tau} = \Gamma \nabla^2 \frac{\delta \mathcal{F}}{\delta \phi}, \tag{10}$$

where $\mathcal{F}$ is the free-energy functional defined by Eq. (2) with the free-energy densities given by Eqs. (3) and (4) for the one- and two-mode models, respectively. This form for the one-mode approximation has recently been theoretically motivated in the context of dynamical DFT [33]. To minimize the number of parameters, it is useful to rewrite the equations in dimensionless form. For the two-mode model, we define the dimensionless parameters

$$\epsilon = -\frac{a}{\lambda q_0^8}, \tag{11}$$

$$R_1 = \frac{r_1}{q_0^4}, \tag{12}$$

$$Q_1 = \frac{q_1}{q_0}, \tag{13}$$

where we set $Q_1 = |\vec{K}_{200}|/|\vec{K}_{111}| = \sqrt{4/3}$ for fcc (i.e., Q_1 equal to the ratio of the magnitudes of the $\langle 200 \rangle$ and $\langle 111 \rangle$ RLVs). We also define the dimensionless variables

$$\vec{r}' = q_0 \vec{r}, \tag{14}$$

$$\psi = \sqrt{\frac{g}{\lambda q_0^8}}\phi, \tag{15}$$

$$t = \Gamma \lambda q_0^7 \tau, \tag{16}$$

$$F = \frac{g}{\lambda^2 q_0^{13}} \mathcal{F}. \tag{17}$$

Substituting the above definitions into Eqs. (2) and (4) yields the dimensionless form

$$\frac{\partial \psi}{\partial t} = \nabla^2 \frac{\delta F}{\delta \psi}, \tag{18}$$

with the free-energy functional

$$F = \int d\vec{r} f(\psi), \tag{19}$$

and free-energy density

$$f = \frac{\psi}{2}\{-\epsilon + (\nabla^2 + 1)^2[(\nabla^2 + Q_1^2)^2 + R_1]\}\psi + \frac{\psi^4}{4}, \tag{20}$$

where we have dropped the prime symbol on the dimensionless spatial coordinate vector $\vec{r}'$ for brevity. Even though most of the paper focuses on the two-mode model, we also compute in Sec. V the elastic constants for the standard one-mode PFC model. For this model, we use the same scaling as in Ref. [15] with the parameter

$$\epsilon = -\frac{a}{\lambda q_0^4}, \tag{21}$$

and dimensionless variables

$$\psi = \sqrt{\frac{g}{\lambda q_0^4}}\phi, \tag{22}$$

$$t = \Gamma \lambda q_0^3 \tau, \tag{23}$$

$$F = \frac{g}{\lambda^2 q_0^5} \mathcal{F}, \tag{24}$$

where $\vec{r}'$ is defined by Eq. (14). Substituting the above forms into Eqs. (2) and (3) yields (after dropping the prime symbol on $\vec{r}'$) the dimensionless form of the one-mode PFC Eqs. (18) and (19) with

$$f = \frac{\psi}{2}[-\epsilon + (\nabla^2 + 1)^2]\psi + \frac{\psi^4}{4}. \tag{25}$$

B. Phase diagram

The phase diagram of the two-mode PFC model is obtained by computing the free-energy density as a function of the mean density $\bar{\psi}$ in solid and liquid, denoted by $f_s(\bar{\psi})$, and

$f_l(\bar{\psi})$, respectively, and then using a standard common tangent construction to obtain equilibrium values of $\bar{\psi}$ in solid ($\bar{\psi}_s$) and liquid ($\bar{\psi}_l$).

Since the density is constant in the liquid, f_l is obtained directly from Eq. (20)

$$f_l(\bar{\psi}_l) = -\left(\epsilon - \frac{16}{9} - R_1\right)\frac{\bar{\psi}_l^2}{2} + \frac{\bar{\psi}_l^4}{4}. \tag{26}$$

For small ϵ, the solid free-energy density can be well approximated by only considering the contribution of the $\langle 111\rangle$ and $\langle 200\rangle$ RLVs. Accordingly, the crystal density field is expanded in the form

$$\psi(\vec{r}) \approx \bar{\psi} + \sum_{\vec{K}_i=\langle 111\rangle} A_i e^{i\vec{K}_i\cdot\vec{r}} + \sum_{\vec{K}'_j=\langle 200\rangle} B_j e^{i\vec{K}'_j\cdot\vec{r}} \approx \bar{\psi} + 8A_s \cos qx \cos qy \cos qz + 2B_s(\cos 2qx + \cos 2qy + \cos 2qz), \tag{27}$$

where we have used the fact that all density waves have the same amplitude in the crystal ($|A_i|=A_s$ and $|B_i|=B_s$) and the magnitude of the principal RLVs are unity in our dimensionless units so ($q=1/\sqrt{3}$). The parameters A_s and B_s are solved by substituting Eq. (27) into Eqs. (19) and (20) and by minimizing the resulting free-energy F with respect to A_s and B_s. This minimization yields the solid free-energy density

$$f_s(\bar{\psi}_s) = 4(-\epsilon + 3\bar{\psi}_s^2)A_s^2 + 3\left(-\epsilon + 3\bar{\psi}_s^2 + \frac{R_1}{9}\right)B_s^2 + 72\bar{\psi}_s A_s^2 B_s + 144A_s^2B_s^2 + 54A_s^4 + \frac{45}{2}B_s^4 - \frac{\epsilon}{2}\bar{\psi}_s^2 + \frac{R_1}{2}\bar{\psi}_s^2 + \frac{8}{9}\bar{\psi}_s^2 + \frac{1}{4}\bar{\psi}_s^4, \tag{28}$$

where A_s and B_s are themselves functions of $\bar{\psi}$. The coexistence densities $\bar{\psi}_s$ and $\bar{\psi}_l$ are computed numerically using the standard common tangent construction, which consists of equating the chemical potentials $f'_s(\bar{\psi}_s)=f'_l(\bar{\psi}_l)=\mu_E$ and grand potentials $f_s(\bar{\psi}_s)-\mu_E\bar{\psi}_s=f_l(\bar{\psi}_l)-\mu_E\bar{\psi}_l$ of the two phases. It is also necessary to compute the solid free-energy curve for bcc since the latter can have a lower free energy than fcc for some regions of the phase diagram. The bcc free-energy density was obtained by expanding the crystal density field using a one-mode approximation, which only involves $\langle 110\rangle$ RLVs as in Ref. [15], and substituting this expansion into the two-mode model defined by Eqs. (19) and (20).

An example of the phase diagram for $R_1=0.05$ is shown in Fig. 1, where we also show for completeness the hexagonal and stripe phases. As desired, we obtain a large ϵ range of fcc-liquid coexistence. For small ϵ, however, bcc becomes favored over fcc. A common tangent construction using fcc and bcc free-energy curves shows that the density range of bcc-fcc coexistence is extremely narrow for small values of ϵ and cannot be resolved on the scale of Fig. 1. As will be explained later in Sec. III C, the range of ϵ where bcc is favored depends on the value of R_1. In the limit $R_1 \gg 1$, the two-mode model reduces to the standard one-mode model after a simple rescaling of parameters, which can be easily seen by comparing Eqs. (20) and (25). Hence, increasing R_1 reduces the contribution of the second mode. Conversely, reducing R_1 increases the contribution of this mode and tends to favor the fcc structure, which extends to smaller ϵ for smaller R_1. In the extreme case where $R_1=0$, the region of fcc-liquid coexistence extends all the way to vanishingly small ϵ as shown in Fig. 2.

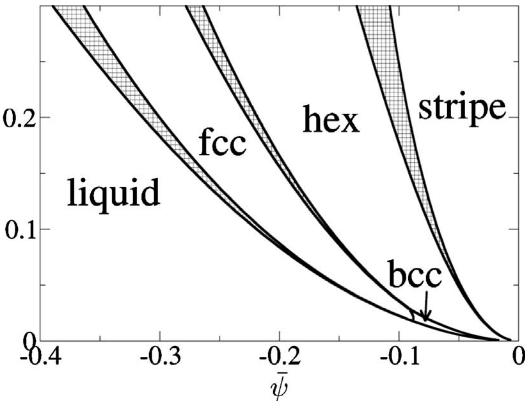

FIG. 1. Phase diagram of the two-mode PFC model for $R_1=0.05$ computed using two-mode and one-mode expansions of the crystal density field for fcc and bcc, respectively.

C. Numerical examples

We now demonstrate the feasibility of the model with some numerical examples of fcc polycrystalline growth and (111) twin growth. The PFC conserved dynamics governed by Eq. (18) with the free-energy defined by Eqs. (19) and (20) was solved using the semi-implicit pseudospectral scheme given by Eq. (A2) in Appendix of Ref. [34]. We used the parameters $R=0$ and $\epsilon=0.0082$ obtained from our fit of pure Ni presented later in Sec. IV, together with the grid

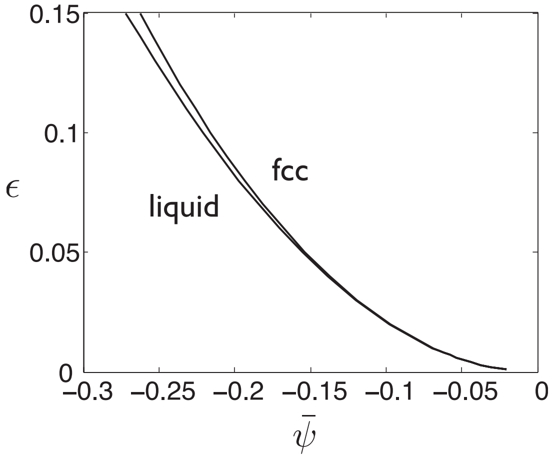

FIG. 2. Phase diagram of the two-mode PFC model showing only the fcc-solidus and liquidus for the case $R_1=0$ where fcc-liquid coexistence extends to vanishingly small ϵ.

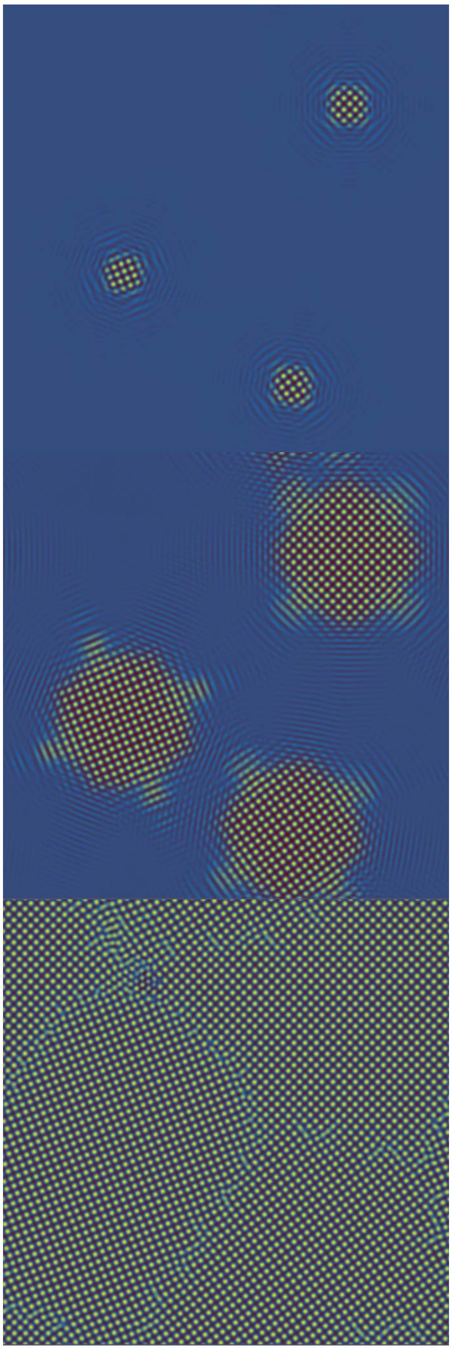

FIG. 3. (Color online) Simulation of polycrystalline solidification starting from three seeded fcc crystals in a supercooled liquid. The system is fully periodic, and the snapshots are taken at dimensionless times $t=5\times10^2$, 3×10^3, and 10^5. The parameters are $R=0$, $\epsilon=0.0082$, and $\bar{\psi}=-0.06$. Lighter shades (yellow online) correspond to higher densities and darker shades (blue online) to lower densities. This is the (001) lattice plane.

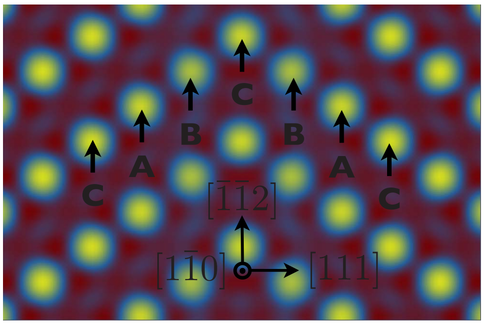

FIG. 4. (Color online) Simulation of an equilibrium coherent (111) twin boundary for $R=0$, $\epsilon=0.0082$. Lighter shades (yellow online) correspond to higher densities and darker shades (blue online) to lower densities.

spacing $\Delta x=\Delta y=\Delta z=2\pi\sqrt{3}/16$, which determines the number of Fourier modes, and the time step $\Delta t=0.5$. For this value of R and ϵ, the computations presented in the next section show that the size of the solid-liquid coexistence region is extremely small, i.e., $\bar{\psi}_s-\bar{\psi}_l$ is two orders of magnitude smaller than $(\bar{\psi}_s+\bar{\psi}_l)/2$ as can already be seen from the phase diagram in Fig. 2, and $\bar{\psi}_s\approx\bar{\psi}_l\approx-0.0627$.

The first example in Fig. 3 shows the growth of small fcc crystallites of different orientations for a value of $\bar{\psi}=-0.06 > \bar{\psi}_s$ that is well inside the stable fcc-solid region of the phase diagram. The crystallites grow as expected until they collide to form grain boundaries. The second example in Fig. 4 shows a (111) twin crystal at coexistence and for a system size chosen such that a twin crystal with two stacking faults fits perfectly the periodic boundary conditions in all directions without any liquid present. A computation of the excess free energy of this twin boundary given in the Appendix to this paper yields a value of approximately 30 mJ/m^2 that falls within the range of values typically reported in the literature for fcc metals. Figure 5 then shows the growth of the same twin crystal in a supercooled liquid for a much larger system with $\bar{\psi}=-0.06$.

III. AMPLITUDE EQUATIONS

A. Scalings

In this section, we analyze in more detail the properties of the model by expanding the free energy in terms of the amplitudes of density waves. In the one-mode bcc case analyzed

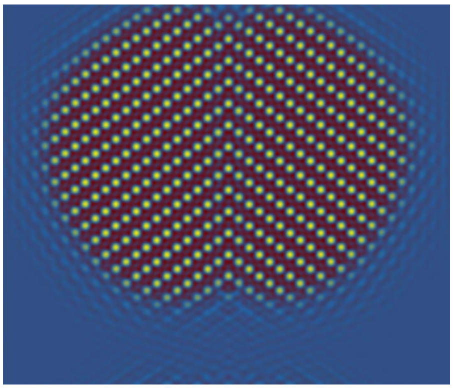

FIG. 5. (Color online) Simulation of the growth of a twin crystal in a supercooled liquid for $R=0$, $\epsilon=0.0082$, and $\bar{\psi}=-0.06$. Lighter shades (yellow online) correspond to higher densities and darker shades (blue online) to lower densities. The orientation is the same as Fig. 4.

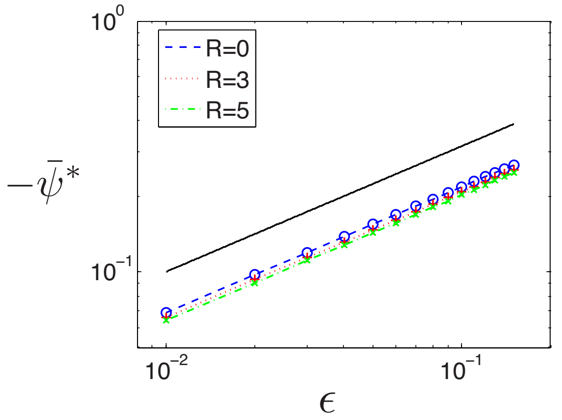

FIG. 6. (Color online) Plots of $\bar{\psi}^* \equiv \frac{1}{2}(\bar{\psi}_s + \bar{\psi}_l)$ versus ϵ for different values of R, with $\bar{\psi}_s$ and $\bar{\psi}_l$ calculated from the common tangent construction. Fits to the numerical results of the form $\bar{\psi}^* = \psi_c \epsilon^{1/2}$ yield for $R=0$, $\psi_c=-0.6902$, for $R=3$, $\psi_c=-0.6578$, and for $R=5$, $\psi_c=-0.6396$. The solid black line has a slope of exactly 1/2 on this log-log plot showing that the mean density $\sim\epsilon^{1/2}$.

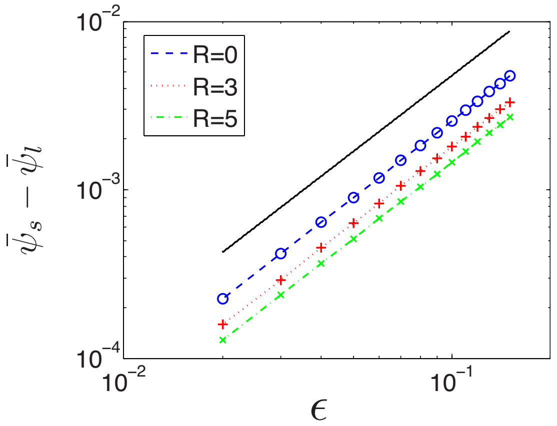

FIG. 7. (Color online) Plots of $\bar{\psi}_s - \bar{\psi}_l$ versus ϵ for the same values of R as in Fig. 6, with $\bar{\psi}_s$ and $\bar{\psi}_l$ calculated from the common tangent construction. The solid black line has a slope of exactly 3/2 on this log-log plot showing that the density difference between solid and liquid $\sim\epsilon^{3/2}$.

in Ref. [15], a similar expansion exploited the fact that the amplitude of ⟨110⟩ density waves scales as $\epsilon^{1/2}$ in the small ϵ limit. In the present case, the expansion is rendered more difficult by the presence of two different sets of density waves with amplitudes A_s and B_s corresponding to ⟨111⟩ and ⟨200⟩ RLVs, respectively. Therefore, it is not *a priori* obvious how A_s and B_s should scale in the small ϵ limit. If R_1 is kept constant, the bcc structure turns out to always be favored in the small ϵ limit as apparent in the phase diagram of Fig. 1. Consequently, a small ϵ amplitude expansion that captures the fcc structure cannot be carried out at fixed R_1. However, if R_1 is decreased proportionally to ϵ by imposing the additional scaling $R_1=\epsilon R$, both A_s and B_s scale as $\epsilon^{1/2}$, thereby making a rigorous expansion possible. This expansion may seem artificial since the phase diagram of Fig. 1 is computed at fixed R_1. However, as we show below, the results of this expansion can be used to understand the small ϵ structure of the phase diagram, in particular the relative stability of fcc and bcc.

To demonstrate the feasibility of this expansion, we first analyze fcc-liquid coexistence for small ϵ with the scaling $R_1=\epsilon R$. The equilibrium densities are calculated using the common tangent construction described in the previous section. To make the dependence of the coexistence densities on ϵ explicit, we make a log-log plot of the mean coexistence density $\bar{\psi}^* \equiv \frac{1}{2}(\bar{\psi}_l + \bar{\psi}_s)$ versus ϵ for three different values of R. The results in Fig. 6 show that the mean coexistence density scales as $\epsilon^{1/2}$. Next in Fig. 7, we show a log-log plot of the density difference between solid and liquid versus ϵ for the same three values of R. The results show that $\bar{\psi}_s - \bar{\psi}_l \sim \epsilon^{3/2}$. Together, these two log-log plots show that, in the small ϵ limit, the two-mode PFC model exhibits a weak first-order freezing transition where the size of the solid-liquid coexistence region is at the order of $\epsilon^{3/2}$ that is much smaller than the mean value of the density $\sim\epsilon^{1/2}$.

B. Free-energy functional

The above scalings suggest that we can expand the crystal density field in powers of $\epsilon^{1/2}$ as

$$\psi(\vec{r}) = \psi_0(\vec{r})\epsilon^{1/2} + \psi_1(\vec{r})\epsilon + \psi_2(\vec{r})\epsilon^{3/2} + \cdots, \tag{29}$$

and expand accordingly the average densities

$$\bar{\psi}_l = \psi_{l0}\epsilon^{1/2} + \psi_{l1}\epsilon + \psi_{l2}\epsilon^{3/2} + \cdots, \tag{30}$$

and

$$\bar{\psi}_s = \psi_{s0}\epsilon^{1/2} + \psi_{s1}\epsilon + \psi_{s2}\epsilon^{3/2} + \cdots, \tag{31}$$

in the liquid and solid, respectively. The numerically determined scaling relations $(\bar{\psi}_l + \bar{\psi}_s)/2 \sim \epsilon^{1/2}$ and $\bar{\psi}_s - \bar{\psi}_l \sim \epsilon^{3/2}$ then imply that

$$\psi_{l0} = \psi_{s0} \equiv \psi_c, \tag{32}$$

and

$$\psi_{l1} = \psi_{s1} = 0. \tag{33}$$

Next, to carry out the amplitude expansion, we start from the equilibrium equation $\delta F/\delta\psi = \mu_E$, where μ_E is the equilibrium value of the chemical potential. With F defined by Eqs. (19) and (20), we obtain

$$\mu_E = -\epsilon\psi + (\nabla^2 + 1)[(\nabla^2 + Q_1^2)^2 + \epsilon R]\psi + \psi^3. \tag{34}$$

We substitute the small ϵ expansion of the density field Eq. (29) into Eq. (34) and collect terms with the same power of ϵ. We find at the order $\epsilon^{1/2}$

$$(\nabla^2 + 1)^2(\nabla^2 + Q_1^2)^2\psi_0 = Q_1^4\psi_c, \tag{35}$$

which has the solution

$$\psi_0 = \psi_c + \sum_i A_i^0 e^{i\vec{K}_i\cdot\vec{r}} + \sum_j B_j^0 e^{i\vec{K}_j'\cdot\vec{r}}, \tag{36}$$

where the summations are over ⟨111⟩ and ⟨200⟩ RLVs, respectively, and $|\vec{K}_i|=1$, $|\vec{K}_j'|=\sqrt{4/3}$, in our scaled units. At order ϵ, we obtain

$$(\nabla^2 + 1)^2(\nabla^2 + Q_1^2)^2\psi_1 = 0, \tag{37}$$

which has the solution

$$\psi_1=\sum_i A_i^1 e^{i\vec{K}_i\cdot\vec{r}}+\sum_j B_j^1 e^{i\vec{K}'_j\cdot\vec{r}}, \tag{38}$$

and collecting the terms at order $\epsilon^{3/2}$ yields

$$\begin{aligned}-\psi_0+(\nabla^2+1)^2(\nabla^2+Q_1^2)^2\psi_2+R(\nabla^2+1)^2\psi_0+(\psi_0)^3&=-\psi_c\\ &+Q_1^4\psi_{l2}+R\psi_c+(\psi_c)^3.\end{aligned} \tag{39}$$

Since $(\nabla^2+1)^2(\nabla^2+Q_1^2)^2\psi_2$ gives a vanishing contribution for all density waves associated with sets $\{K_i\}$ and $\{K'_j\}$, all remaining terms $\sim e^{i\vec{K}_i\cdot\vec{r}}$ and $e^{i\vec{K}'_j\cdot\vec{r}}$ must balance each other in order for a solution of Eq. (39) to exist. For example, the condition that the coefficients of $e^{i\overrightarrow{K_{111}}\cdot\vec{r}}$ balance each other yields

$$\begin{aligned}&(-1+3\psi_c^2)A_{111}^0+(3|A_{111}^0|^2+6|A_{1\bar{1}1}^0|^2+6|A_{11\bar{1}}^0|^2+6|A_{1\bar{1}\bar{1}}^0|^2\\ &\quad+6|B_{200}^0|^2+6|B_{020}^0|^2+6|B_{002}^0|^2)A_{111}^0+6\psi_c(A_{\bar{1}11}^0B_{200}^0\\ &\quad+A_{1\bar{1}1}^0B_{020}^0+A_{11\bar{1}}^0B_{002}^0)+6A_{11\bar{1}}^0A_{1\bar{1}1}^0A_{\bar{1}11}^0+6A_{\bar{1}\bar{1}1}^0B_{200}^0B_{020}^0\\ &\quad+6A_{\bar{1}1\bar{1}}^0B_{200}^0B_{002}^0+6A_{1\bar{1}\bar{1}}^0B_{002}^0B_{020}^0=0,\end{aligned} \tag{40}$$

and requiring that the coefficients of $e^{i\overrightarrow{K_{200}}\cdot\vec{r}}$ balance each other yields in turn

$$\begin{aligned}&(-1+3\psi_c^2+R(-Q_1^2+1)^2)B_{200}^0+(6|A_{111}^0|^2+6|A_{1\bar{1}1}^0|^2\\ &\quad+6|A_{11\bar{1}}^0|^2+6|A_{1\bar{1}\bar{1}}^0|^2+3|B_{200}^0|^2+6|B_{020}^0|^2+6|B_{002}^0|^2)B_{200}^0\\ &\quad+6\psi_c(A_{11\bar{1}}^0A_{1\bar{1}1}^0+A_{111}^0A_{1\bar{1}\bar{1}}^0)+6(B_{020}^0A_{1\bar{1}1}^0A_{1\bar{1}\bar{1}}^0\\ &\quad+B_{002}^0A_{1\bar{1}\bar{1}}^0A_{11\bar{1}}^0+B_{0\bar{2}0}^0A_{11\bar{1}}^0A_{111}^0+B_{00\bar{2}}^0A_{1\bar{1}1}^0A_{111}^0)=0.\end{aligned} \tag{41}$$

The above solvability condition must be satisfied independently for each reciprocal lattice vector. This yields a set of 14 coupled amplitude equations that are straightforward to obtain. From those amplitude equations, it is useful to express the free energy of the system measured from its constant value in the liquid, defined as the difference ΔF^{AE}, as a functional of the density wave amplitudes A_i^0 and B_i^0. This quantity can be expressed solely in terms of the amplitudes of density waves owing to the property that the size of the coexistence region ($\sim\epsilon^{3/2}$) is much smaller than the mean density ($\sim\epsilon^{1/2}$) in the small ϵ limit. Since the amplitudes are not conserved order parameters, the equilibrium state simply corresponds to a minimum of this free energy. Hence the amplitude equations must be equivalent to

$$\frac{\delta\Delta F^{AE}}{\delta A_i^{0*}}=0, \tag{42}$$

and

$$\frac{\delta\Delta F^{AE}}{\delta B_i^{0*}}=0. \tag{43}$$

For the case where the amplitudes are spatially uniform, we obtain the free-energy density

$$\begin{aligned}\Delta F^{AE}/V\equiv\Delta f^{AE}&=(-1+3\psi_c^2)(|A_{111}^0|^2+|A_{11\bar{1}}^0|^2+|A_{1\bar{1}1}^0|^2+|A_{1\bar{1}\bar{1}}^0|^2)+(-1+3\psi_c^2+R(-Q_1^2+1)^2)(|B_{200}^0|^2+|B_{020}^0|^2+|B_{002}^0|^2)\\ &\quad+\frac{3}{2}(|A_{111}^0|^4+|A_{11\bar{1}}^0|^4+|A_{1\bar{1}1}^0|^4+|A_{1\bar{1}\bar{1}}^0|^4+|B_{200}^0|^4+|B_{020}^0|^4+|B_{002}^0|^4)+6(|A_{111}^0|^2|A_{1\bar{1}1}^0|^2+|A_{111}^0|^2|A_{11\bar{1}}^0|^2\\ &\quad+|A_{111}^0|^2|A_{1\bar{1}\bar{1}}^0|^2+|A_{1\bar{1}1}^0|^2|A_{11\bar{1}}^0|^2+|A_{1\bar{1}1}^0|^2|A_{1\bar{1}\bar{1}}^0|^2+|A_{11\bar{1}}^0|^2|A_{1\bar{1}\bar{1}}^0|^2)+6(|B_{200}^0|^2|B_{020}^0|^2+|B_{200}^0|^2|B_{002}^0|^2+|B_{020}^0|^2|B_{002}^0|^2)\\ &\quad+6(|A_{111}^0|^2+|A_{11\bar{1}}^0|^2+|A_{1\bar{1}1}^0|^2+|A_{1\bar{1}\bar{1}}^0|^2)(|B_{200}^0|^2+|B_{020}^0|^2+|B_{002}^0|^2)+6\psi_c(A_{111}^0A_{1\bar{1}\bar{1}}^0B_{\bar{2}00}^0+A_{111}^0A_{\bar{1}1\bar{1}}^0B_{0\bar{2}0}^0\\ &\quad+A_{111}^0A_{\bar{1}\bar{1}1}^0B_{00\bar{2}}^0+A_{11\bar{1}}^0A_{1\bar{1}1}^0B_{\bar{2}00}^0+A_{11\bar{1}}^0A_{\bar{1}11}^0B_{0\bar{2}0}^0+A_{11\bar{1}}^0A_{\bar{1}\bar{1}\bar{1}}^0B_{002}^0+A_{1\bar{1}1}^0A_{\bar{1}11}^0B_{00\bar{2}}^0+A_{1\bar{1}1}^0A_{\bar{1}\bar{1}\bar{1}}^0B_{020}^0+A_{1\bar{1}\bar{1}}^0A_{\bar{1}1\bar{1}}^0B_{002}^0\\ &\quad+A_{1\bar{1}\bar{1}}^0A_{\bar{1}\bar{1}1}^0B_{020}^0+A_{\bar{1}11}^0A_{\bar{1}\bar{1}\bar{1}}^0B_{200}^0+A_{\bar{1}1\bar{1}}^0A_{\bar{1}\bar{1}1}^0B_{200}^0)+6A_{11\bar{1}}^0A_{1\bar{1}1}^0A_{\bar{1}11}^0A_{\bar{1}\bar{1}\bar{1}}^0+6A_{\bar{1}\bar{1}1}^0A_{\bar{1}1\bar{1}}^0A_{1\bar{1}\bar{1}}^0A_{111}^0+6A_{\bar{1}\bar{1}1}^0A_{\bar{1}\bar{1}\bar{1}}^0B_{200}^0B_{020}^0\\ &\quad+6A_{\bar{1}1\bar{1}}^0A_{\bar{1}\bar{1}\bar{1}}^0B_{200}^0B_{002}^0+6A_{1\bar{1}\bar{1}}^0A_{\bar{1}\bar{1}\bar{1}}^0B_{002}^0B_{020}^0+6A_{\bar{1}11}^0A_{111}^0B_{00\bar{2}}^0B_{0\bar{2}0}^0+6A_{11\bar{1}}^0A_{111}^0B_{\bar{2}00}^0B_{0\bar{2}0}^0+6A_{1\bar{1}1}^0A_{111}^0B_{\bar{2}00}^0B_{00\bar{2}}^0\\ &\quad+6A_{\bar{1}11}^0A_{\bar{1}1\bar{1}}^0B_{200}^0B_{0\bar{2}0}^0+6A_{1\bar{1}\bar{1}}^0A_{1\bar{1}1}^0B_{\bar{2}00}^0B_{020}^0+6A_{\bar{1}11}^0A_{\bar{1}\bar{1}1}^0B_{200}^0B_{00\bar{2}}^0+6A_{11\bar{1}}^0A_{1\bar{1}\bar{1}}^0B_{\bar{2}00}^0B_{002}^0+6A_{1\bar{1}1}^0A_{\bar{1}\bar{1}1}^0B_{00\bar{2}}^0B_{020}^0\\ &\quad+6A_{11\bar{1}}^0A_{\bar{1}1\bar{1}}^0B_{002}^0B_{0\bar{2}0}^0.\end{aligned} \tag{44}$$

In general, the above free-energy density is a multivariate function of the 14 amplitudes A_i^0 and B_i^0 of different density waves, and cannot be represented graphically in a simple way. However, the free-energy barrier between solid and liq-

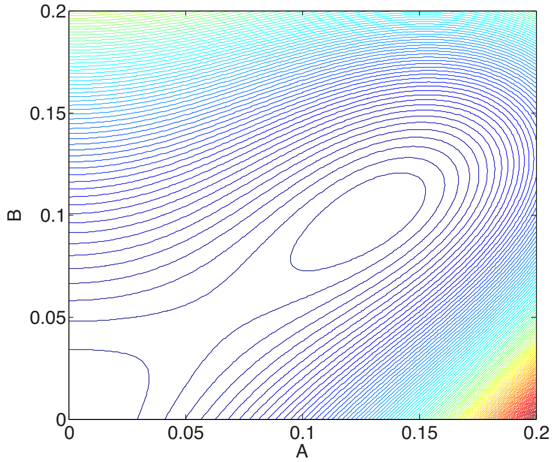

FIG. 8. (Color online) Free-energy landscape defined by Eq. (45) as a function of the amplitudes A and B of $\langle 111\rangle$ and $\langle 200\rangle$ density waves, respectively, for $R=0$ and the corresponding coexistence value $\psi_c=-0.6902$ where the solid and liquid minima have the same height.

uid can be made explicit by assuming that all the $\langle 111\rangle$ and all the $\langle 200\rangle$ density waves have the same amplitude (i.e., $A_i^0=A$ and $B_i^0=B$, respectively). In this isotropic approximation (see [15] for the bcc analog), the free-energy density (scaled by ϵ^{-2} as described below) becomes

$$\Delta f^{AE}=4(-1+3\psi_c^2)A^2+3[-1+3\psi_c^2+R(-Q_1^2+1)^2]B^2 \\ +54A^4+\frac{45}{2}B^4+144A^2B^2+72\psi_c A^2 B. \qquad (45)$$

This expression can also be obtained by evaluating directly the difference between the solid and liquid free-energy densities, $\Delta f^{AE}=\epsilon^{-2}(f_s-f_l)$, with f_l and f_s given by Eqs. (26) and (28), respectively, and the substitutions $\bar{\psi}_s=\bar{\psi}_l=\psi_c\epsilon^{1/2}$, $A_s=A\epsilon^{1/2}$, and $B_s=B\epsilon^{1/2}$. For the parameters $R=0$ and ψ_c calculated from the common tangent construction, we plot in Fig. 8 the free-energy landscape as a function of amplitudes A and B. The free-energy landscape exhibits two minima that correspond to the stable liquid and solid phases. The above amplitude equation calculation shows that the two-mode PFC model describes well solid-liquid coexistence with a well-defined free-energy barrier between solid and liquid.

We have only treated here the case where the amplitudes are spatially uniform to characterize the bulk free-energy landscape. A more general free-energy functional that includes gradient terms would be necessary to treat the case where the amplitudes are spatially varying. Such a functional could then be used to compute the excess free-energy of the solid-liquid interface and its anisotropy, as done previously for bcc [15]. Those computations will be presented elsewhere.

C. Relative stability of fcc and bcc

So far, we have only examined the possibility of fcc-liquid coexistence. However, the phase diagram of Fig. 1 shows that bcc can have a lower free energy than fcc for small enough ϵ if R_1 is finite. We now use the amplitude equations to understand the relative stability of fcc and bcc. As a first step, it is useful to re-examine the scaling of the mean density that is controlled by the parameter ψ_c. We computed previously the equilibrium solid and liquid densities using the common tangent construction, from which we obtained the scalings $(\bar{\psi}_s+\bar{\psi}_l)/2=\psi_c\epsilon^{1/2}$, which defines ψ_c, and $\psi_s-\bar{\psi}_l\sim\epsilon^{3/2}$, which shows that the size of the density difference between solid and liquid can be neglected in the small ϵ limit. We can also compute ψ_c more directly from Eq. (45) by requiring

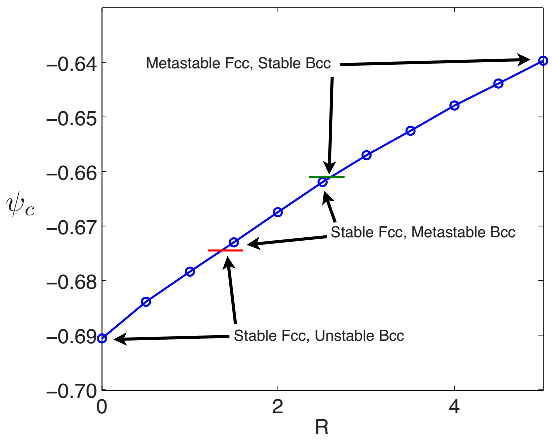

FIG. 9. (Color online) ψ_c as a function of R showing different ranges of bcc or fcc metastability, stability, or instability.

$$\frac{\partial\Delta f^{AE}}{\partial A}=\frac{\partial\Delta f^{AE}}{\partial B}=0, \qquad (46)$$

and

$$\Delta f^{AE}=0, \qquad (47)$$

with all the above relations evaluated at the equilibrium values of A and B in the solid. Equation (46) stems from the requirement that the solid amplitudes must correspond to a free-energy minimum, which fixes those amplitudes uniquely as functions of ψ_c. Equation (47), in turn, is the requirement that the free energies of solid and liquid must be equal in equilibrium, which fixes ψ_c uniquely for a given R. A plot of ψ_c versus R obtained in this way using Eqs. (46) and (47) is shown in Fig. 9.

The relationship between ψ_c and R, denoted by $\psi_c(R)$, can now be used to assess the relative stability of bcc and fcc. To obtain an analogous expression to Eq. (45) for bcc, we substitute into the two-mode free-energy functional defined by Eqs. (19) and (20), the one-mode expansion of the bcc crystal density field in terms of principal set of $\langle 110\rangle$ density waves

$$\psi(\vec{r})\approx\epsilon^{1/2}\psi_c+4\epsilon^{1/2}A(\cos qx\cos qy+\cos qx\cos qz \\ +\cos qy\cos qz), \qquad (48)$$

where $q=1/\sqrt{2}$. We obtain

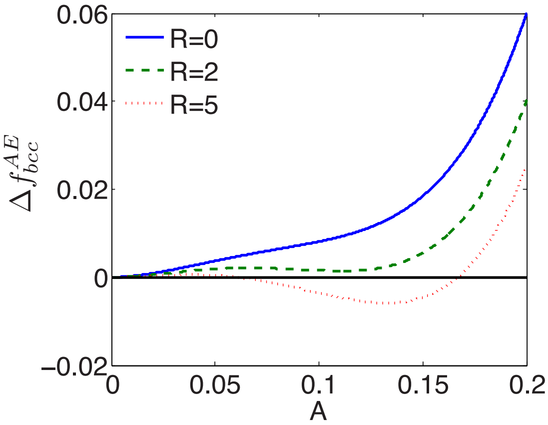

FIG. 10. (Color online) Plots of free-energy density of bcc relative to the liquid, $\Delta f^{AE}_{\text{bcc}}$, as a function of the amplitude A of $\langle 110\rangle$ density waves for different values of R. When the value of $\Delta f^{AE}_{\text{bcc}}$ corresponding to the solid bcc free-energy minimum is negative, bcc is favored over fcc. As R decreases, bcc first becomes metastable with respect to fcc and then unstable as the local solid free-energy minimum disappears.

$$\Delta f^{AE}_{\text{bcc}} = 6(3\psi_c^2 - 1)A^2 + 48\psi_c A^3 + 135A^4, \tag{49}$$

where A now denotes the amplitude of $\langle 110\rangle$ density waves and we have used the subscript "bcc" to distinguish this free energy difference between bcc and liquid from the one between fcc and liquid, Δf^{AE}, defined by Eq. (45). By definition, $\Delta f^{AE}=0$ for solid fcc in equilibrium with the liquid. Therefore, to assess the relative stability of bcc and fcc, we can plot $\Delta f^{AE}_{\text{bcc}}$ defined by Eq. (49) versus A and check if the value corresponding to the solid bcc minimum is above (below) zero in which case fcc (bcc) has a lower free energy than bcc (fcc). Such plots shown in Fig. 10 show that bcc becomes metastable with respect to fcc and then unstable (with the disappearance of the local solid bcc free-energy minimum) as R is decreased. A detailed study as a function of R shows that bcc first becomes metastable for $R<R_c$ where $R_c=2.68$ and then unstable as R is decreased below a second threshold value (≈ 1.43), giving rise to the three different stability regimes as a function of R shown in Fig. 9. Translated in terms of the phase diagram constructed at fixed R_1, this implies that bcc becomes favored over fcc when $\epsilon < \epsilon_c$ where

$$\epsilon_c = \frac{R_1}{R_c}. \tag{50}$$

For $R_1=0.05$, the above expression predicts $\epsilon_c \approx 0.019$ that is in good quantitative agreement with the phase diagram of Fig. 1. As R_1 increases, ϵ_c increases and the switch from stable bcc-liquid to fcc-liquid coexistence moves to higher values of ϵ in the phase diagram. Even though we have not systematically studied the size of the fcc-bcc coexistence region, we find that it is much narrower than the size of the solid-liquid coexistence region for the parameters of Fig. 1.

IV. PARAMETER DETERMINATION

In this section, we derive expressions to relate the two-mode PFC model parameters to material parameters by extending our previous approach for bcc [15]. As a first step, we match the peak liquid structure factor properties of the two-mode PFC model to the standard expression from classical DFT. The expression for the PFC liquid structure factor is obtained by varying ψ around its liquid value, $\psi=\bar{\psi}_l+\delta\psi$, and evaluating the corresponding variation $\Delta\mathcal{F}$ of the dimensional free-energy difference between solid and liquid using Eqs. (2) and (4), and the relation (15) between ϕ and ψ. Dropping terms of $\delta\psi$ higher than quadratic order, we obtain

$$\Delta\mathcal{F}_{\text{PFC}} = \frac{\lambda q_0^8}{g}\int d\vec{r}\left[\frac{\delta\psi}{2}[a + 3\bar{\psi}_l^2\lambda q_0^8 + \lambda(\nabla^2+q_0^2)^2((\nabla^2+q_1^2)^2 + r_1)]\delta\psi\right]. \tag{51}$$

Substituting the Fourier transform,

$$\delta\psi = \int \frac{d\vec{k}}{(2\pi)^{3/2}}\delta\psi_k e^{i\vec{k}\cdot\vec{r}}, \tag{52}$$

we obtain

$$\begin{aligned}\Delta\mathcal{F}_{\text{PFC}} &= \frac{\lambda q_0^8}{g}\int\int \frac{d\vec{k}d\vec{k}'}{(2\pi)^3}\frac{\delta\psi_k\delta\psi_{k'}}{2}\Big\{\{a + 3\bar{\psi}_l^2\lambda q_0^8 + \lambda(-k^2 + q_0^2)^2[(-k^2+q_1^2)^2 + r_1]\}\int d\vec{r}e^{i(\vec{k}+\vec{k}')\cdot\vec{r}}\Big\}\\ &= \frac{\lambda q_0^8}{g}\int d\vec{k}\frac{\delta\psi_k\delta\psi_{-k}}{2}\{a + 3\bar{\psi}_l^2\lambda q_0^8 + \lambda(-k^2+q_0^2)^2[(-k^2 + q_1^2)^2 + r_1]\}.\end{aligned} \tag{53}$$

A second expression for the free-energy of a spatially inhomogeneous liquid is obtained from classic DFT

$$\Delta\mathcal{F}_{\text{DFT}} = \frac{k_BT}{2}\int\int d\vec{r}d\vec{r}', \quad \delta n(\vec{r}')\left[\frac{\delta(\vec{r}-\vec{r}')}{n_0} - C(|\vec{r}-\vec{r}'|)\right]\delta n(\vec{r}'), \tag{54}$$

where

$$\delta n(\vec{r}) = n(\vec{r}) - n_0 = \delta\phi(\vec{r}) = \sqrt{\frac{\lambda q_0^8}{g}}\delta\psi(\vec{r}), \tag{55}$$

and

$$C(k) = n_0\int d\vec{r}C(|\vec{r}|)e^{-i\vec{k}\cdot\vec{r}} \tag{56}$$

is the Fourier transform of the direct correlation function. Fourier transforming again, we obtain

$$\Delta\mathcal{F}_{\mathrm{DFT}} = \frac{\lambda q_0^8}{g}\frac{k_BT}{2n_0}\int d\vec{k}\,\delta\psi_k\delta\psi_{-k}[1-C(k)]. \tag{57}$$

Equating $\Delta\mathcal{F}_{\mathrm{PFC}}=\Delta\mathcal{F}_{\mathrm{DFT}}$ and using the expression for the liquid structure factor $S(k)=1/[1-C(k)]$, we obtain

$$S(k) = \frac{k_BT}{n_0\{a+3\lambda q_0^8\bar{\psi}_l^2+\lambda(-k^2+q_0^2)^2[(-k^2+q_1^2)^2+r_1]\}}. \tag{58}$$

By evaluating the above expression at the peak of the liquid structure factor, we obtain

$$a+3\lambda q_0^8\bar{\psi}_l^2 = \frac{k_BT}{n_0S(q_0)}, \tag{59}$$

or, using Eq. (11) and the relationship $\bar{\psi}_l=\psi_c\epsilon^{1/2}$,

$$\epsilon = \frac{-k_BT}{n_0S(q_0)\lambda q_0^8(1-3\psi_c^2)}. \tag{60}$$

A second relation is now needed to determine ϵ and λ independently. To obtain it, we substitute Eq. (58) into the relation $C(k)=[S(k)-1]/S(k)$ and compute the second derivative of $C(k)$ evaluated at the peak of the liquid structure factor to obtain

$$\lambda = -\frac{k_BTC''(q_0)}{8n_0q_0^6\left(\frac{1}{9}+\epsilon R\right)}. \tag{61}$$

Equations (60) and (61) combined now give

$$\epsilon = \frac{8}{9[q_0^2S(q_0)C''(q_0)(1-3\psi_c^2)-8R]}, \tag{62}$$

and

$$\lambda = \frac{-9k_BTC''(q_0)}{8n_0q_0^6} + \frac{9k_BTR}{n_0S(q_0)(1-3\psi_c^2)q_0^8}. \tag{63}$$

In addition, the relation Eq. (55) between the real and dimensionless densities expresses

$$g = \frac{\lambda q_0^8A_s^2}{n_0^2u_s^2}, \tag{64}$$

in terms of the solid amplitude A_s of the first q_0 mode. The two solid amplitudes A_s and B_s can be computed for a given R by using the scaling relations $A_s=\epsilon^{1/2}A$ and $B_s=\epsilon^{1/2}B$ where A and B are the equilibrium values of the scaled amplitudes in solid. The latter are obtained, together with ψ_c (Fig. 9), by using the conditions Eqs. (46) and (47) with ΔF^{AE} defined by Eq. (45).

For a given R, Eqs. (62)–(64) fix the three parameters ϵ, λ, and g of the PFC model uniquely in terms of peak liquid structure factor properties, $S(q_0)$ and $C''(q_0)$, where $q_0=|\vec{K}_{111}|$ here, and the solid-density wave amplitude $u_s=u_{111}$. This still leaves the freedom to vary R within the range where fcc is stable with respect to bcc (Fig. 9). Varying R changes the shape of the liquid structure factor as shown in Fig. 12 and decreasing R below some threshold produces a second peak at $q_1=|\vec{K}_{200}|$, and generally increases the contribution of the second mode. Thus, decreasing R increases the amplitude of the second mode u_{200} as shown in Fig. 11. For simplicity, we used the value $R=0$ that yields a reasonable fit of this amplitude for pure Ni. The other input parameters computed by Hoyt [36] using the embedded-atom method (EAM) potential of Foiles, Baskes, and Daw [37] (FBD) are given in Table I. The density wave amplitudes are calculated using the relation $u_i=\exp(-K_i^2/4a)$, which assumes that the crystal density field is a sum of Gaussians centered around each fcc lattice site. The value of a is obtained from the expressions for the root-mean-square displacement of atoms in the solid $\sqrt{\langle|\vec{r}|^2\rangle}=3/(2a)$ derived from this density field. For the value $\sqrt{\langle|\vec{r}|^2\rangle}\approx 0.298$ Å from MD simulations, we obtain $u_{111}=\exp(-K_{111}^2/4a)=0.6639$ and $u_{200}=\exp(-K_{111}^2/4a)=0.5791$.

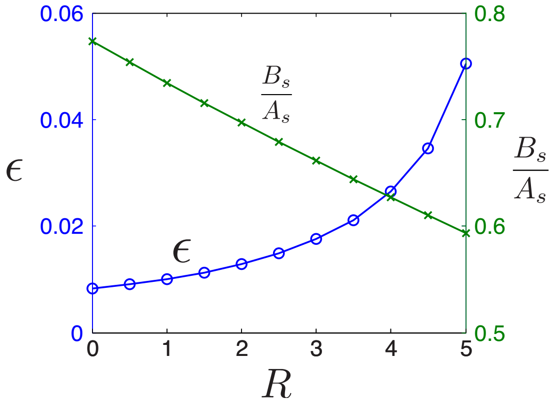

FIG. 11. (Color online) Plots showing the variation with R of ϵ calculated by Eq. (62) and the ratio B_s/A_s of the solid amplitudes of the second and first modes calculated by the conditions Eqs. (46) and (47) with Δf^{AE} defined by Eq. (45).

It should be noted that, with the present fitting procedure, the two-mode PFC model only reproduces the correct shape

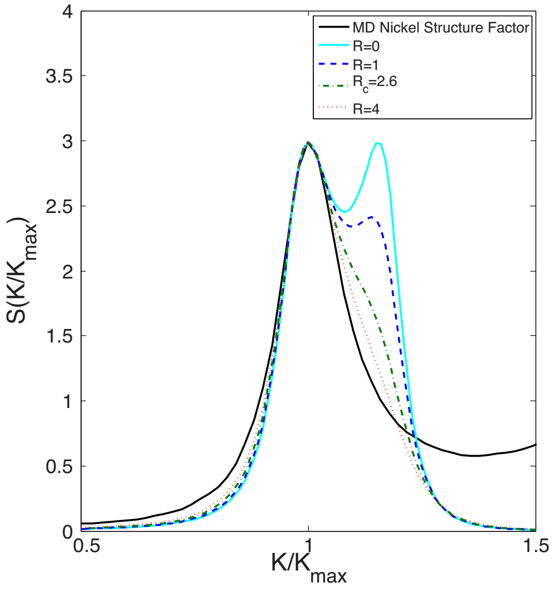

FIG. 12. (Color online) Liquid structure factor of the PFC model and from MD simulations of pure Ni [36].

TABLE I. Input parameters for the PFC model computed from MD simulations of pure Ni [36] using the FBD EAM potential [37] and corresponding PFC parameters.

MD input parameters	Value	PFC parameters	Value
$q_0=K_{111}$ (Å^{-1})	3.0376	λ (eV Å^{11})	0.026
n_0 (Å^{-3})	0.0801	g (eV Å^9)	8.53
$C''(q_0)$ (Å^2)	−9.1579	ψ_c	−0.6902
$S(q_0)$	2.9898	R	0
T_M (K)	1811	ϵ	0.0082
u_{111}	0.6639	u_{111}	0.6639
u_{200}	0.5791	u_{200}	0.5136

of the main peak of the liquid structure factor. The second peak is spurious and is only used to increase the amplitude of the second mode to some desired value. Since the second mode is critical to obtain solid-liquid coexistence, the lack of realism of the structure factor outside of the first peak is a limitation of the present two-mode model. The liquid structure factor could in principle be made more realistic by shifting the second peak to larger wave vector and reducing its amplitude, which would couple the principal ⟨111⟩ RLVs to other sets such as ⟨222⟩ and ⟨311⟩. However, larger k modes require a finer mesh and are computationally more costly to resolve. Whether such a fit would offer specific advantages remains to be investigated.

V. ELASTIC CONSTANTS

In this section, we derive analytical expressions for the elastic constants of the two-mode PFC model. We compare the results to MD computations of elastic constants at the melting point for parameters of fcc Ni. For completeness, we also carry out the same comparison for the standard one-mode PFC model for parameters of bcc Fe. Following the same approach as in Ref. [2], we obtain the elastic constants by deforming the lattice from its ideal structure and computing the corresponding change of free-energy density. We consider three different deformations

$$\psi_1(\vec{r}) = \psi[x/(1+\xi), y/(1+\xi), z/(1+\xi)], \tag{65}$$

$$\psi_2(\vec{r}) = \psi[x/(1+\xi), y/(1-\xi), z], \tag{66}$$

$$\psi_3(\vec{r}) = \psi(x+\xi y, y, z), \tag{67}$$

of the two-mode crystal density field We compute the change of free-energy density

$$\Delta f_i = \frac{F_i}{V_i} - f_s, \tag{68}$$

where f_s is the free-energy density of the unperturbed solid and F_i is the free-energy integrated over the perturbed unit cell of volume V_i with

$$\frac{F_1}{V_1} = \frac{1}{V(1+\xi)^3}\int_0^{a(1+\xi)}\int_0^{a(1+\xi)}\int_0^{a(1+\xi)} f[\psi_1(\vec{r})]dV,$$

$$\frac{F_2}{V_2} = \frac{1}{V(1-\xi^2)}\int_0^{a}\int_0^{a(1-\xi)}\int_0^{a(1+\xi)} f[\psi_2(\vec{r})]dV,$$

$$\frac{F_3}{V_3} = \frac{1}{V}\int_0^{a}\int_0^{a}\int_{-\xi y}^{a-\xi y} f[\psi_3(\vec{r})]dV,$$

where $dV = dxdydz$, a is the lattice spacing, and $V=a^3$ is the unperturbed unit cell volume.

The scaled density wave amplitudes of the perturbed solid, denoted here by A^i and B^i, generally differ from the scaled amplitudes of the unperturbed solid, A^0 and B^0, by an amount proportional to ξ^2. However, the correct elastic constants can nonetheless be obtained by evaluating Eq. (68) using the unperturbed amplitudes because A^0 and B^0 correspond to free-energy minima of the bulk free-energy density of the amplitude equations in the small ϵ limit. Namely, Taylor expanding Δf_i around the unperturbed state and using the fact that $|A^i - A^0| \sim |B^i - B^0| \sim \xi^2$, we obtain for small ϵ

$$\Delta f_i = f_s[(\epsilon^{1/2}A^i),(\epsilon^{1/2}B^i)] - f_s[(\epsilon^{1/2}A^0),(\epsilon^{1/2}B^0)] + \frac{1}{2}\frac{d^2}{d\xi^2}\left(\frac{F_i}{V_i}\right)_{\{A^i=A^0,B^i=B^0\}}\xi^2 + \ldots, \tag{69}$$

at leading order in ξ^2, with f_l and f_s given by Eqs. (26) and (28), respectively, where $\bar{\psi}_s = \bar{\psi}_l = \psi_c \epsilon^{1/2}$. Furthermore, using the fact that $\Delta f^{AE} \equiv \epsilon^{-2}(f_s - f_l)$ and that f_l is independent of the amplitudes, we obtain

$$\Delta f_i = \epsilon^2[\Delta f^{AE}(\{A^i\},\{B^i\}) - \Delta f^{AE}(\{A^0\},\{B^0\})] + \frac{1}{2}\frac{d^2}{d\xi^2}\left(\frac{F_i}{V_i}\right)_{\{A^i=A^0,B^i=B^0\}}\xi^2, \tag{70}$$

Since A^0 and B^0 are minima of ΔF^{AE},

$$\left(\frac{\partial \Delta f^{AE}}{\partial A^i}\right)_{\{A^i=A^0,B^i=B^0\}} = 0,$$

$$\left(\frac{\partial \Delta f^{AE}}{\partial B^i}\right)_{\{A^i=A^0,B^i=B^0\}} = 0, \tag{71}$$

and again using the fact that $|A^i - A^0| \sim |B^i - B^0| \sim \xi^2$, $\Delta f^{AE}(\{A^i\},\{B^i\}) - \Delta f^{AE}(\{A^0\},\{B^0\})$ gives a vanishing contribution to order ξ^2, and we obtain finally

$$\Delta f_i = \frac{1}{2}\frac{d^2}{d\xi^2}\left(\frac{F_i}{V_i}\right)_{\{A^i=A^0,B^i=B^0\}}\xi^2. \tag{72}$$

A. Fcc elastic constants for the two-mode model

Using Eqs. (65)–(68) with the two-mode crystal density field $\psi(\vec{r})$ defined by Eq. (27), evaluated with unperturbed amplitudes as explained above, and the free-energy density $f[\psi(\vec{r})]$ defined by Eq. (20), we obtain the dimensionless elastic constants

$$\Delta f_1 = \left(\frac{3}{2}\tilde{C}_{11} + 3\tilde{C}_{12}\right)\xi^2 = (\alpha+\beta)\xi^2, \tag{73}$$

TABLE II. Comparison of elastic constants at the melting point predicted by the two-mode PFC model for fcc Ni and the one-mode PFC model for bcc Fe and MD simulations [39].

Quantity	PFC fcc	MD fcc	PFC bcc	MD bcc
C_{11} (GPa)	112.5	155.4	90.0	128.0
C_{12} (GPa)	33.1	124.7	45.0	103.4
C_{44} (GPa)	33.1	66.0	45.0	63.9
Bulk Modulus (GPa) $(C_{11}+2C_{12})/3$	59.6	134.9	60.0	111.6

$$\Delta f_2 = (\tilde{C}_{11} - \tilde{C}_{12})\xi^2 = \frac{2}{3}\beta\xi^2, \tag{74}$$

$$\Delta f_3 = \frac{\tilde{C}_{44}}{2}\xi^2 = (\alpha/9 + \delta)\xi^2, \tag{75}$$

where we have defined

$$\alpha = 16(1 - 2Q_1^2 + Q_1^4 + R_1)A_s^2, \tag{76}$$

$$\beta = \frac{8}{27}(284 - 315Q_1^2 + 81Q_1^4 + 81R_1)B_s^2, \tag{77}$$

$$\delta = \frac{8}{9}R_1 B_s^2. \tag{78}$$

We can set $R_1 \approx 0$ in the above expression since $R_1 \ll 1$ for typical model parameters where the fcc lattice is favored. With only the principle $\langle 111 \rangle$ RLVs ($B_s=0$), all three elastic constants are equal $\tilde{C}_{11}=\tilde{C}_{12}=\tilde{C}_{44}=2\alpha/9$, which gives a vanishing tetragonal shear modulus $\tilde{C}'=(\tilde{C}_{11}-\tilde{C}_{12})/2$. The inclusion of the $\langle 200 \rangle$ RLVs, however, raises the value of $\tilde{C}_{11}$, which becomes

$$\tilde{C}_{11} = \frac{2}{9}\alpha\left(1 + 4\frac{B_s^2}{A_s^2}\right),$$

while leaving the values of $\tilde{C}_{12}$ and $\tilde{C}_{44}$ unchanged, thereby making $\tilde{C}'$ finite as desired. Finally, converting back to dimensional units using the relation $C_{ij}=(\lambda^2 q_0^{16}/g)\tilde{C}_{ij}$, we obtain

$$C_{11} = -\frac{4}{9}n_0 k_B T C''(K_{111})q_0^2 u_{111}^2\left(1 + 4\frac{u_{200}^2}{u_{111}^2}\right), \tag{79}$$

and

$$C_{12} = C_{44} = -\frac{4}{9}n_0 k_B T C''(K_{111})q_0^2 u_{111}^2. \tag{80}$$

The elastic constants computed with the parameters of Table I are compared to the predictions of MD simulations in Table II. The MD simulations for fcc Fe and bcc Ni were carried out using the EAM potentials from Mendelev, Han, Srolovitz, Ackland, Sun, and Asta MH(SA)^2 [38], and Foiles, Baskes and Daw [37], respectively. The same EAM potentials were used to compute the input parameters for the PFC model and the elastic constants. The input parameters for Fe are the same as in Ref. [35]. The input parameters for Ni were computed by Hoyt [36]. The elastic constants for both Fe and Ni were computed by Foiles [39]. Their values at the melting point are smaller than at zero temperature as shown by Foiles for a different Ni EAM potential [40].

B. bcc elastic constants for the one-mode model

For the one-mode model, we use again Eqs. (65)–(68) with the one-mode bcc crystal density field

$$\psi(\vec{r}) \approx \bar{\psi} + 4A_s(\cos qx \cos qy + \cos qx \cos qz + \cos qy \cos qz), \tag{81}$$

where A_s is the amplitude of the unperturbed solid, $q = 1/\sqrt{2}$ and the free-energy density $f[\psi(\vec{r})]$ defined by Eq. (25). We obtain

$$\Delta f_1 = \left(\frac{3}{2}\tilde{C}_{11} + 3\tilde{C}_{12}\right)\xi^2 = \alpha_{\mathrm{bcc}}\xi^2, \tag{82}$$

$$\Delta f_2 = (\tilde{C}_{11} - \tilde{C}_{12})\xi^2 = \frac{\alpha_{\mathrm{bcc}}}{6}\xi^2, \tag{83}$$

$$\Delta f_3 = \frac{\tilde{C}_{44}}{2}\xi^2 = \frac{\alpha_{\mathrm{bcc}}}{12}\xi^2, \tag{84}$$

where $\alpha_{\mathrm{bcc}}=24A_s^2$. This yields the dimensionless elastic constants $\tilde{C}_{11}=2\tilde{C}_{12}=2\tilde{C}_{44}=8A_s^2$. Finally, converting back to dimensional units using the relation $C_{ij}=(\lambda^2 q_0^8/g)\tilde{C}_{ij}$, we obtain

$$C_{11} = 2C_{12} = 2C_{44} = -n_0 k_B T C''(K_{110})q_0^2 u_{110}^2. \tag{85}$$

The elastic constants computed with the input parameters of Table III for bcc Fe are compared to the predictions of MD simulations in Table II.

VI. TWO-DIMENSIONAL SQUARE LATTICE

As an example of application of the two-mode model to other lattice structures, we briefly examine the example of two-dimensional square lattices. Those lattices are obtained by coupling $\langle 10 \rangle$ and $\langle 11 \rangle$ density waves with $Q_1=\sqrt{2}$, as demonstrated previously by Lifshitz and Petrich [19] for a modified Swift-Hohenberg model that corresponds to the $R_1=0$ limit of the present two-mode model. The liquid free-energy density is given by

TABLE III. Input parameters for the PFC model computed from MD simulations of pure Fe [35] using the EAM potential from MH(SA)^2 [38] and corresponding PFC parameters.

MD input parameters	Value	PFC parameters	Value
$q_0=K_{110}$ (Å^{-1})	2.985	λ (eV Å^7)	0.291
n_0 (Å^{-3})	0.0765	g (eV Å^9)	9.705
$C''(q_0)$ (Å^2)	−10.40	ϵ	0.0923
$S(q_0)$	3.012	u_{110}	0.72
T_M (K)	1771		
u_{110}	0.72		

$$f_l^{sq}(\bar{\psi}_l) = -(\epsilon - 4 - R_1)\frac{\bar{\psi}_l^2}{2} + \frac{\bar{\psi}_l^4}{4}, \tag{86}$$

and the solid free-energy density is obtained by substituting the two-mode crystal density field

$$\psi(\vec{r}) \approx \bar{\psi} + 2A_s(\cos x + \cos y) + 4B_s(\cos x \cos y) \tag{87}$$

into the free-energy functional defined by Eqs. (19) and (20) with $Q_1=\sqrt{2}$, which yields

$$f_s^{sq}(\bar{\psi}_s) = 2(-\epsilon + 3\bar{\psi}_s^2)A_s^2 + 2(-\epsilon + 3\bar{\psi}_s^2 + R_1)B_s^2 + 24\bar{\psi}_s A_s^2 B_s + 36A_s^2B_s^2 + 9A_s^4 + 9B_s^4 - \frac{\epsilon}{2}\bar{\psi}_s^2 + \frac{R_1}{2}\bar{\psi}_s^2 + 2\bar{\psi}_s^2 + \frac{1}{4}\bar{\psi}_s^4. \tag{88}$$

For $R_1=0$, we obtain $\psi_c=-0.6782$ numerically from a log-log plot of the mean equilibrium density versus ϵ similar to Fig. 6 which is determined from the common tangent construction. The feasibility of the two-model to model polycrystalline solidification and grain boundaries is illustrated in Fig. 13. As for fcc, the second mode turns out to be essential to obtain physically meaningful elastic constants. Following the same procedure as for fcc in the last section (with deformations of the unit cell now constrained to the $x-y$ plane) we obtain

$$\Delta f_1^{sq} = (\tilde{C}_{11} + \tilde{C}_{12})\xi^2 = (\alpha_{sq} + \beta_{sq})\xi^2, \tag{89}$$

$$\Delta f_2^{sq} = (\tilde{C}_{11} - \tilde{C}_{12})\xi^2 = (\alpha_{sq} + \Lambda_{sq})\xi^2, \tag{90}$$

$$\Delta f_3^{sq} = \frac{\tilde{C}_{44}}{2}\xi^2 = \delta_{sq}\xi^2, \tag{91}$$

with

$$\alpha_{sq} = 8(1 - 2Q_1^2 + Q_1^4 + R_1)A_s^2, \tag{92}$$

$$\beta_{sq} = 8(58 - 37Q_1^2 + 5Q_1^4 + 5R_1)B_s^2, \tag{93}$$

$$\Lambda_{sq} = 8R_1B_s^2, \tag{94}$$

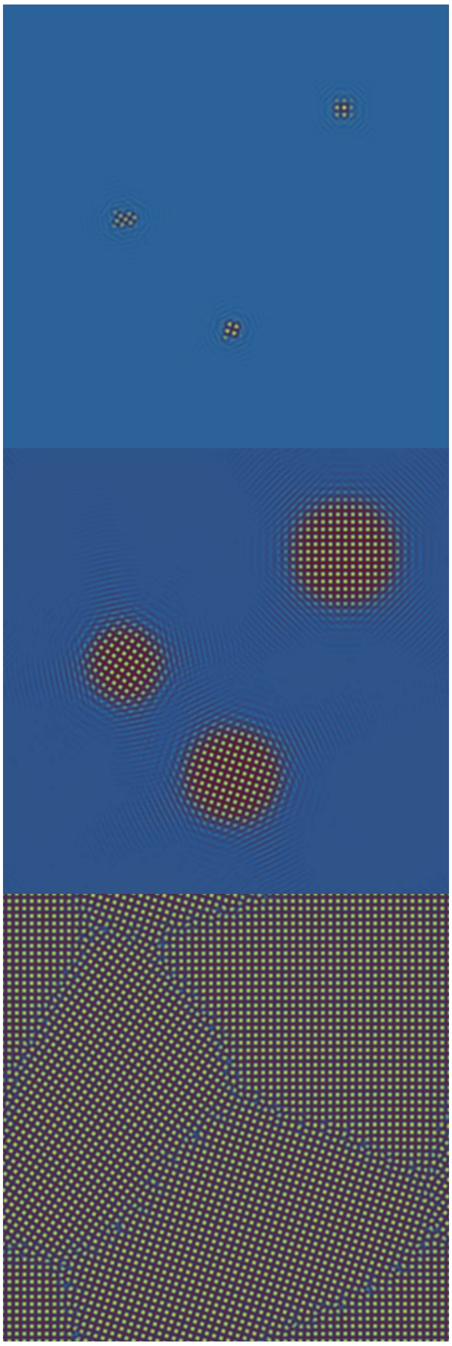

FIG. 13. (Color online) Example of polycrystalline solidification for two-dimensional square lattices. The snapshots are at dimensionless times $t=10$, 100, and 1000. The parameters are $\epsilon=0.15$, $R_1=0$, $Q_1=\sqrt{2}$, and $\bar{\psi}=-0.23$. Lighter shades (yellow online) correspond to higher densities and darker shades (blue online) to lower densities.

$$\delta_{sq} = 4(32 - 21Q_1^2 + 3Q_1^4 + 3R_1)B_s^2. \tag{95}$$

Again we look in the limit $R_1 \approx 0$. This yields the dimensionless elastic constants

$$\tilde{C}_{11} = \alpha_{sq} + \beta_{sq}/2, \tag{96}$$

$$\tilde{C}_{12} = \beta_{sq}/2, \tag{97}$$

$$\tilde{C}_{44} = 2\delta. \tag{98}$$

These relations show that the one-mode crystal density field consisting only of a superposition of $\langle 10 \rangle$ density waves ($B_s=0$) yield vanishing shear moduli, which become finite with the inclusion of the second mode.

VII. CONCLUDING REMARKS

In summary, we have presented a two-mode PFC model with a phase diagram that includes different temperature ranges for bcc-liquid and fcc-liquid coexistence. The relative sizes of these ranges can be changed by varying one model parameter that controls the relative magnitudes of the amplitudes of the two modes, corresponding to [111] and [200] density waves, respectively. We have shown that the free-energy landscape for fcc-liquid coexistence has a double-well structure with a finite free-energy barrier between solid and liquid in the plane of the amplitudes of the two modes. We have demonstrated the feasibility of the model with some numerical examples of fcc polycrystalline growth and twin growth, as well as for two-dimensional square lattices.

At a more quantitative level, we have determined the model parameters by fitting the peak liquid structure factor properties [$S(q_0)$ and $C''(q_0)$] and solid-density wave amplitudes as an extension of our previous study of bcc Fe [15]. Furthermore, we have derived analytical expressions for the elastic constants. With input values for those parameters from MD simulations of pure Ni, we have found that the PFC model elastic constants are in reasonable agreement with MD results given the simplicity of the model, which neglects the contributions of many other modes that are present in a realistic description of the crystal density field. Those expressions also stress the necessity of having at least two distinct modes to obtain physically meaningful values of the elastic constants for fcc in the physically relevant small ϵ-limit of the PFC model, which is also true for square lattices. We have found that the standard one-mode PFC model also predicts reasonable values of the elastic constants for pure bcc Fe, and we have argued that any one- or two-mode model will predict similar elastic constants for bcc and fcc with the same peak liquid structure factor properties and solid-density wave amplitudes

Finally, while the numerical examples focused on crystal growth, it might also be possible to use the two-mode PFC model to study the bcc/fcc martensitic transformation, which has been modeled by other phase-field approaches that make use of structural order parameters (see Refs. [41,42] and references therein). The ability to vary the relative stability of fcc and bcc crystal structures, which was demonstrated here, should prove particularly useful for this application.

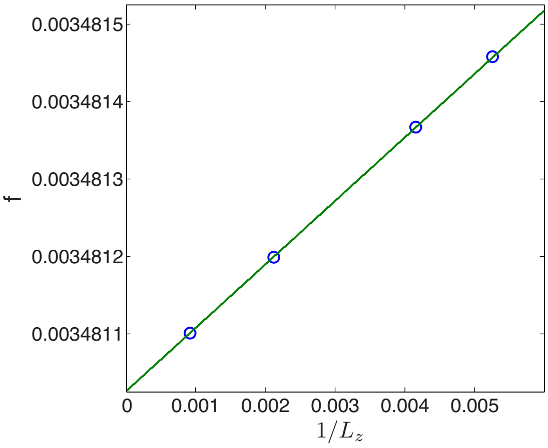

FIG. 14. (Color online) Plot of free-energy density versus inverse of the system length perpendicular to the twin boundary used to compute its excess free-energy.

ACKNOWLEDGMENTS

This work was supported by DOE (Grant No. DE-FG02-07ER46400) and the DOE sponsored Computational Materials Science Network program. We thank Mark Asta and Jeff Hoyt for valuable exchanges and Stephen Foiles for providing values of the elastic constants computed from molecular dynamics simulations.

APPENDIX: TWIN BOUNDARY ENERGY

We computed the coherent (111) twin boundary energy using the method put forth in Ref. [34], which exploits the dependence of the free energy on system size. We performed simulations for four different lengths L_z along the axis perpendicular to the boundary. By plotting the bulk free-energy density f against the inverse of this length (Fig. 14), we then extracted the boundary energy from the slope of this plot using the relation

$$f = f_s(\bar{\psi}) + 2\frac{\tilde{\gamma}_{\rm twin}}{L_z}, \tag{A1}$$

where $f_s(\bar{\psi})$ is the free-energy density of a perfect crystal. This method turns out to be more accurate than computing directly the excess free energy of the boundary for a fixed system size [34]. This calculation gives twice the boundary energy since there are two boundaries in our periodic system. We convert the result to dimensional units through, $\gamma_{\rm twin} = (\lambda^2 q_0^{15}/g)\tilde{\gamma}_{\rm twin}$, which yields the reasonable value of 29.9 mJ/m^2 for the same Ni parameters used to compute the elastic constants.

[1] K. R. Elder, M. Katakowski, M. Haataja, and M. Grant, Phys. Rev. Lett. **88**, 245701 (2002).

[2] K. R. Elder and M. Grant, Phys. Rev. E **70**, 051605 (2004).

[3] K. R. Elder, N. Provatas, J. Berry, P. Stefanovic, and M. Grant, Phys. Rev. B **75**, 064107 (2007).

[4] P. M. Stefanovic, M. Haataja, and N. Provatas, Phys. Rev. Lett. **96**, 225504 (2006).

[5] J. Berry, M. Grant, and K. R. Elder, Phys. Rev. E **73**, 031609 (2006).

[6] K.-A. Wu and P. W. Voorhees, Phys. Rev. B **80**, 125408 (2009).

[7] T. V. Ramakrishnan and M. Yussouff, Phys. Rev. B **19**, 2775 (1979).

[8] A. D. J. Haymet and D. W. Oxtoby, J. Chem. Phys. **74**, 2559 (1981).

[9] B. B. Laird, J. D. McCoy, and A. D. J. Haymet, J. Chem. Phys. **87**, 5449 (1987).

[10] Y. Singh, Phys. Rep. **207**, 351 (1991).

[11] P. Harrowell and D. Oxtoby, J. Chem. Phys. **80**, 1639 (1984).

[12] Y. C. Shen and D. Oxtoby, J. Chem. Phys. **105**, 6517 (1996).

[13] Y. C. Shen and D. Oxtoby, J. Chem. Phys. **104**, 4233 (1996).

[14] J. Berry, K. R. Elder, and M. Grant, Phys. Rev. E **77**, 061506 (2008).

[15] K.-A. Wu and A. Karma, Phys. Rev. B **76**, 184107 (2007).

[16] A. Jaatinen, C. V. Achim, K. R. Elder, and T. Ala-Nissila, Phys. Rev. E **80**, 031602 (2009).

[17] J. Swift and P. C. Hohenberg, Phys. Rev. A **15**, 319 (1977).

[18] M. C. Cross and P. C. Hohenberg, Rev. Mod. Phys. **65**, 851 (1993).

[19] R. Lifshitz and D. M. Petrich, Phys. Rev. Lett. **79**, 1261 (1997).

[20] J. F. Lutsko, Phys. Rev. E **74**, 021121 (2006).

[21] B. M. Mladek, D. Gottwald, G. Kahl, M. Neumann, and C. N. Likos, Phys. Rev. Lett. **96**, 045701 (2006).

[22] J. F. Lutsko and M. Baus, J. Phys.: Condens. Matter **3**, 6547 (1991).

[23] M. Hasegawa and K. Ohno, J. Phys.: Condens. Matter **9**, 3361 (1997).

[24] M. G. Day and A. Hellawell, Proc. R. Soc. London, Ser. A **305**, 473 (1968).

[25] R. E. Napolitano, H. Meco, and C. Yung, JOM **56**, 16 (2004).

[26] S. Henry, G.-U. Gruen, and M. Rappaz, Metall. Mater. Trans. A **35**, 2495 (2004).

[27] R. Spatschek and A. Karma, eprint arXiv:org/abs/1002.1580 (unpublished).

[28] K.-A. Wu, Ph.D. thesis, Northeastern University, 2006.

[29] H. Sakaguchi and H. R. Brand, Phys. Lett. A **227**, 209 (1997).

[30] Y. Enomoto, K. Oba, Y. Hayase, and T. Ohta, J. Phys. Soc. Jpn. **70**, 2939 (2001).

[31] A. A. Golovin and A. A. Nepomnyashchy, Phys. Rev. E **67**, 056202 (2003).

[32] F. C. Larché and J. W. Cahn, Acta Metall. **33**, 331 (1985).

[33] S. van Teeffelen, R. Backofen, A. Voigt, and H. Lowen, Phys. Rev. E **79**, 051404 (2009).

[34] J. Mellenthin, A. Karma, and M. Plapp, Phys. Rev. B **78**, 184110 (2008).

[35] K.-A. Wu, A. Karma, J. J. Hoyt, and M. Asta, Phys. Rev. B **73**, 094101 (2006).

[36] J. J. Hoyt (private communication).

[37] S. M. Foiles, M. I. Baskes, and M. S. Daw, Phys. Rev. B **33**, 7983 (1986).

[38] M. I. Mendelev, S. Han, D. J. Srolovitz, G. J. Ackland, D. Y. Sun, and M. Asta, Philos. Mag. **83**, 3977 (2003).

[39] S. M. Foiles (private communication).

[40] S. M. Foiles, Scr. Mater. **62**, 231 (2010).

[41] Y. Wang and J. Li, Acta Mater. **58**, 1212 (2010).

[42] Y. Wang and A. G. Khachaturyan, Mater. Sci. Eng., A **438**, 55 (2006).